Acta Materialia 133 (2017) 90–99

Contents lists available at ScienceDirect

Acta Materialia

journal homepage: www.elsevier.com/locate/actamat

Full length article

Crystallographic effects on the corrosion of twin roll cast AZ31 Mg alloy sheet

S. Pawar [a], T.J.A. Slater [a], T.L. Burnett [a], X. Zhou [a], G.M. Scamans [b, c], Z. Fan [b], G.E. Thompson [a], P.J. Withers [a, *]

[a] School of Materials, The University of Manchester, Manchester, M13 9PL, UK
[b] The EPSRC Centre – LiME, BCAST, Brunel University, Uxbridge, London, UB8 3PL, UK
[c] Innoval Technology Ltd., Beaumont Close, Banbury, Oxon, OX16 1TQ, UK

ARTICLE INFO

Article history:
Received 21 February 2017
Received in revised form
12 May 2017
Accepted 15 May 2017
Available online 23 May 2017

Keywords:
Automotive sheet
Mg-Al alloy
Micro-galvanic corrosion
Mg dissolution

ABSTRACT

The influence of crystal orientation on the corrosion behaviour of twin roll cast (TRC) AZ31 Mg alloy sheet has been investigated using correlative microscopy and immersion testing in 3.5% NaCl. Corrosion initiates as a consequence of the microgalvanic coupling between cathodic intermetallic phases, including sub-micron sized, rosette-shaped Al_8Mn_5 particles, β-$Mg_{17}(Al,Zn)_{12}$ phase and the Mg matrix. Subsequent development of lateral filiform-like corrosion fronts are observed running along the dendrite arms whilst being constrained by the Al- and Zn-rich interdendritic boundaries. Prolonged immersion showed variable corrosion depths across the surface. By correlating with EBSD analysis, it was confirmed that the corrosion depth is considerably higher in α-Mg grains with non-basal planes on the surface. The severity of attack suffered by α-Mg grains with non-basal planes on the surface is on average twice that for grains with basal or near-basal with planes on the surface. At the same time, corroded α-Mg grains with basal planes on the surface display nanoscale, canyon-like corrosion features developing into the alloy perpendicularly. A mechanism has been proposed to explain the sequential corrosion events.

1. Introduction

Magnesium alloys are attractive candidates for lightweight structural components due to their low density, high specific stiffness and strength [1]. However, Mg-based alloys generally suffer from poor corrosion resistance. This has been largely attributed to the micro-galvanic influence of impurities [2–5], the microstructure and surface modification [6–8]. Specifically, in the case of Mg-Al based alloys, the alloying additions of Al, Zn, Mn, etc., result in the formation of discrete cathodic intermetallics such as Al_xMn_y and β-$Mg_{17}Al_{12}$ phases, etc., which lead to localized micro-galvanic corrosion [8–11].

Mg-Al based alloys have been used for automotive sheet applications, for example, seat frames, instrument panels, etc., with AZ31 being one of the most promising candidates [12–14]. The production routes of metallic alloys affect their properties and the past decades have shown a substantial progress in different methods for production of Mg-based alloys with improved properties. Conventional sheet production involves several processing steps including melting, ingot formation, homogenization, milling, heating, hot rolling and annealing. As the cost of such a multi-step, labour intensive, Mg sheet process is relatively high, an efficient and cost-effective production route is required. The twin roll casting (TRC) process offers several advantages, potentially resulting in significant cost savings [15,16]. The TRC process involves relatively high cooling rates (10^2–10^3 K/s) compared to conventional ingot casting, which results in rapid solidification [17,18]. The typical coarse and non-uniform grain sizes observed in TRC AZ31 Mg alloy are attributed to the formation of α-Mg grains on coarse and randomly distributed MgO particles, which act as nucleating sites [19]. Grain size variations have been reported for Mg alloy sheets of different sheet thicknesses [15]. TRC Mg sheet surfaces have also been reported to exhibit a strong (0001) basal texture, which is also known to adversely affect the tensile properties, especially the formability [16,20,21].

Crystallographic orientation has also been reported to have a profound effect on the corrosion rate and path of Mg and its alloys. EBSD studies on several Mg alloys have shown strong basal textures

* Corresponding author.
E-mail address: p.j.withers@manchester.ac.uk (P.J. Withers).

http://dx.doi.org/10.1016/j.actamat.2017.05.027

arising from the preferred [0001] crystal orientation of Mg grains, which significantly influence the corrosion performance [22–24]. The strong basal texture and the consequent electrochemical anisotropy of Mg surfaces result in increased corrosion resistance [23–26]. The relationship between the crystal orientation and corrosion in commercially pure Mg was demonstrated to be a consequence of the difference in surface energies between the basal (0001), prismatic $(10\bar{1}0)$ and $(11\bar{2}0)$ crystal planes. Theoretically calculated surface energies for the crystal planes of Mg (0001), $(10\bar{1}0)$ and $(11\bar{2}0)$ were reported to be 1.54×10^4, 3.04×10^4 and 2.99×10^4 J mol^{-1} respectively, where the theoretical dissolution rates of $(10\bar{1}0)$ and $(11\bar{2}0)$ crystal planes were suggested to be about 20 times higher than that of the basal (0001) Mg crystal planes [27]. Further, Song et al. showed that Mg grains with a basal orientation in commercially pure Mg are more stable and corrosion resistant, exhibiting a more positive corrosion potential, lower anodic polarization current density, larger impedance, and thinner surface film than grains with a non-basal orientation [28]. On the other hand, formation of filiform-like corrosion morphologies were observed on Mg surfaces when exposed to chromate and chloride solutions [23,29]. McCall et al. [30], showed that Mg (0001) surfaces exhibited pitting corrosion susceptibility and that the $(10\bar{1}0)$ and $(11\bar{2}0)$ crystal surfaces were passive at open circuit potentials. Also, pitting initiated only at potentials slightly anodic to their open circuit potentials, the findings were supported later by Lillard et al.'s simulation analysis [31]. Considering the results reported in the literature, it is clear that the crystal orientation influences the corrosion properties of Mg surfaces.

Most of the observations have been largely conducted on commercially pure Mg and wrought AZ31B Mg specimens, whereas other methods of Mg alloy production can also have crucial ramifications on the resultant Mg alloy surfaces and their properties. AZ31 Mg alloy sheet [16], produced by the conventional TRC process, presents a genuine opportunity to investigate the influence of dendritic and textured microstructures on corrosion properties. In-depth microscopic characterization of corroded surfaces is extremely important in order to determine the structural integrity of such Mg alloy surfaces. Here, a correlative approach bringing together various optical and electron microscopy techniques is applied to study the influence of the crystal orientation of α-Mg grains on the corrosion propagation mechanism. The role of intermetallic phases in the corrosion process for AZ31 has also been carefully considered.

2. Experimental procedure

2.1. Material

AZ31 magnesium alloy sheets of 6 mm thickness were produced by the twin roll casting (TRC) process [16]. Compositional analysis of the TRC AZ31 Mg alloy, shown in Table 1, was carried out using a Perkin-Elmer Optima 5300 dual view inductively coupled plasma atomic emission spectroscope (ICP-AES).

2.2. Specimen preparation

Sample preparation comprises sequential mechanical grinding using successive grades of SiC abrasive papers from 240 to 4000 grits, followed by polishing using 6 μm to ¼ μm diamond pastes with a non-aqueous lubricant and subsequent ultrasonic cleaning in an acetone bath for 15–20 min. The metallographic specimens were etched using an acetic-picral etchant, comprising 5 ml acetic acid +4.2 g picric acid +10 ml distilled water +100 ml (95%) ethanol, for up to 10 s to reveal the microstructural features.

Table 1
Compositional analyses (wt.%) of the twin roll cast AZ31 magnesium alloy obtained by ICP-AES analyses.

Wt.%	Al	Zn	Mn	Si	Fe	Cu	Ni
AZ31	2.9	0.88	0.34	0.02	0.007	0.009	0.004

2.3. Microstructure and texture characterization

Optical microscopy was conducted using a Carl Zeiss light microscope fitted with a polarizer and a digital camera. Scanning electron microscopy (SEM) was undertaken using a Carl Zeiss Ultra 55 FEG-SEM, equipped with an energy dispersive X-ray spectroscopy (EDS) detector, operating at accelerating voltages in the range of 3–20 kV, using secondary (SE) and backscattered electron (BSE) detectors. Additionally, an FEI Magellan FEG-SEM with MAPS™ software was used to capture images from macroscale corroded surfaces at ultra-high resolution, operating at an accelerating voltage of 5 kV and a beam current of 0.4 nA. Secondary electrons were collected using the Everhart Thornley detector (ETD) detector to create the image, and an array of small tiles collected and automatically stitched together using the MAPS software. The array of 750 (25×30) tiles, collected with a step size of 500 nm, provided an ability to investigate the development of the corrosion fronts across the entire (7.5 mm^2) surface, without loss of resolution. Electron backscattered diffraction (EBSD) was conducted on an FEI Magellan FEG-SEM, operating at an accelerating voltage of 20 kV and the EBSD maps were processed using HKL Channel 5 software. Specimens were subjected to EBSD analyses both prior to and after immersion tests. A total of 234 individual EBSD maps (300×300 μm) were obtained, with a step size of 1.5 μm, which were stitched together using Aztec software to create a single snapshot of the corroded surface.

Quantitative texture measurements were performed using X-ray diffraction (XRD), using a Philips X'pert Modular Powder Diffractometer (CuKα) with a scanning range (2θ) of 5°–85°. The resulting peaks were fitted by the X'Pert HighScore software program and the data were used to calculate (0002), $(10\bar{1}0)$ and $(11\bar{2}0)$ pole figures. Thin foils required for imaging in the scanning transmission electron microscope (STEM) were mechanically ground and punched into 3 mm discs with an average thickness of less than 100 μm. The discs were ion beam thinned using a Gatan precision ion polishing system (PIPS) at 5.0 kV and at an incident angle of 4–6°. STEM-EDS elemental mapping was conducted on the FEI Talos instrument, equipped with the Super-XEDS detectors and operated at an accelerating voltage of 200 kV.

2.4. Immersion testing in 3.5% NaCl solution

The immersion testing was conducted at ambient temperature in naturally aerated, near-neutral 3.5% NaCl solution, according to ASTM-G31-72 [32]. The specimens were analysed by SEM-EDS before and after chemical cleaning for 1 min in a boiling solution containing 20% CrO_3 + 1% $AgCrO_4$ [33]. After removal of corrosion products, the specimen surfaces were rinsed in deionized water and acetone, followed by drying in a cool air stream. Measurement of corrosion depths from individual Mg grains after immersion and removal of corrosion products was performed using a 3D Bruker profilometer. The complex dendritic TRC microstructure (Fig. 1a) posed a challenge as the corrosion depths varied across dendrite arms; hence, a series of individual line profiles were taken across the corrosion features in each Mg grain and an average of at least 5 such profiles per Mg grain are plotted in a bar graph, revealing the corrosion depths across several Mg grains.

3. Results

3.1. Microstructural characterization

The etched surface of TRC AZ31 Mg alloy in the optical micrograph of Fig. 1a, shows a dendritic structure of α-Mg grains (HCP, space group P63/mmc, a = 0.32 nm, c = 0.521 nm). Fig. 1b reveals the interior of a single α-Mg grain, displaying the dendrite arms comprising the Mg matrix and the interdendritic regions decorated with a complex distribution of intermetallics, evident in the backscattered electron micrograph. The alloy surface shown in Fig. 1b represents the RD-ND plane of the Mg sheet (RD: rolling direction, ND: normal direction). The sub-micron particle size and the preferential distribution of intermetallics (bright features) on the interdendritic regions (between the dotted lines) are clearly evident in the high magnification SEM image (Fig. 1c). Further, the high angle annular dark field scanning transmission electron micrograph (HAADF-STEM) from a typical interdendritic region (Fig. 1d) and associated EDS maps confirm that the intermetallic particles are mainly β-$Mg_{17}(Al,Zn)_{12}$ phase (Fig. 1e, f, & g) alongside the flower-shaped Al_8Mn_5 intermetallic (Fig. 1g and h). The microscopic analyses presented here highlight the general microstructure of the alloy, consistent with the work reported previously [10,34].

EBSD investigation was conducted prior to immersion, as shown in Fig. 2. The SE image in Fig. 2a reveals the distribution of coarse, as well as fine (60–600 μm) dendritic α-Mg grains possessing irregular shapes, which can be attributed to the nucleation kinetics associated with the TRC process [16]. The texture was measured on the RD-ND plane of the Mg sheet. The inverse pole figure map in Fig. 2b highlights the characteristic texture of the TRC AZ31 Mg alloy sheet. It is evident from the pole figures that the sheet surface possesses a relatively strong basal texture, with a majority of grains oriented with the basal (0002) pole approximately parallel to the ND (red grains in Fig. 2b) in accordance with previous observations [16]. The distribution of a high fraction of α-Mg grains in basal orientation on the TRC surface, evident from the pole figures (Fig. 2c), representing an alloy surface area of 10 mm^2 can be attributed to the influence of rolling conducted during the TRC, which orients the basal crystal planes of the α-Mg grains preferentially towards the roll surface as observed for most as-rolled Mg sheet surfaces [20,21,23,24].

3.2. Initiation of corrosion

This section highlights the initial events occurring on the TRC AZ31 Mg alloy sheet after immersion in 3.5% NaCl solution. It is important to examine the immediate response of the sheet upon electrolyte exposure in order to develop a basic understanding of the corrosion initiation mechanism.

3.2.1. Localized micro-galvanic corrosion

Formation of hydrogen gas bubbles on the alloy surface is evident from the visual observations within several minutes of immersion in 3.5% NaCl [35]. Unreported visual observation after 30 min showed initiation of localized corrosion at the intermetallic particles with consequent hydrogen evolution, which is evident from the dark, spherical, pits arrowed in Fig. 3a. After removal of the corrosion products, cathodic phases such as β-$Mg_{17}(Al,Zn)_{12}$ and Al_8Mn_5 are revealed within the corrosion sites. For example, Fig. 3b and c shows the location and morphology of the intermetallic particle, where the EDS analyses confirmed to be Mn- and Al-rich and based on previous work, it is presumed to be an Al_8Mn_5 intermetallic particle. There is a difference in the contrast of the corroded surface which can be seen between Fig. 3a and b; this is the same region but in Fig. 3b the corrosion product formed during immersion has been removed as described in the experimental section. This was to reveal the underlying microstructure for analysis after corrosion.

3.2.2. Lateral filiform-like corrosion

Gradual development of lateral filiform-like corrosion is observed, which is associated with the localized corrosion pits formed initially at the cathodic intermetallic sites and the surrounding Mg matrix. After 2 h of immersion, it was observed that the corrosion fronts preferentially follow the dendrite arms, as shown in Fig. 4a. The dendrite arms comprising the Mg matrix preferentially corrode; this is anodic and highly corrosion susceptible. These filiform-like corrosion fronts are inhibited at the interdendritic and grain boundaries. As confirmed from the SEM-EDS analyses, these interdendritic and grain boundaries showed relatively high Al and Zn contents compared to the dendrite arms, which makes them relatively resistant and act as corrosion barriers. However, lateral advancement of corrosion fronts into adjacent Mg grains is also observed at some sites. The two individual corrosion

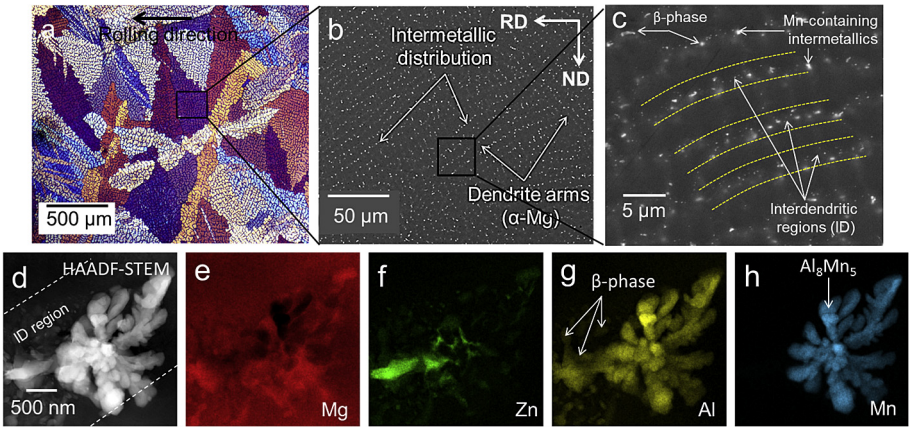

Fig. 1. (a) Optical micrograph under polarized light of the etched surface illustrating the dendritic structure, (b) backscattered electron micrograph highlighting the dendrite arms and distribution of intermetallics within a single α-Mg grain, (c) high magnification SEM image showing the β-phase and Mn-containing intermetallic distribution within the interdendritic (ID) regions (shown within the dotted lines), (d) HAADF-STEM showing discrete intermetallic particles in the ID region along with TEM-EDX maps (e–h) confirming the Mg, Zn, Al and Mn elemental distributions respectively.

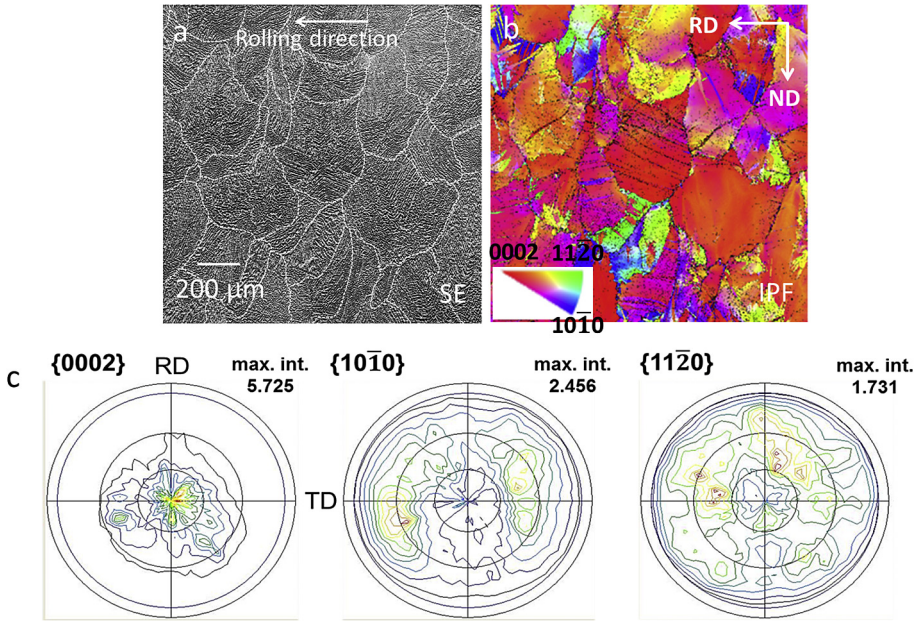

Fig. 2. EBSD analyses of the roll surface, where the texture was measured on the RD-ND plane (also casting direction) (a) SE image, (b) Inverse pole figure map, where the colours of the grains correspond to the crystallographic axes in the stereographic triangle or inverse pole figures, as shown in the inset. (c) {0002}, {10$\bar{1}$0} and {11$\bar{2}$0} pole figures, referring to the RD plane plotted from the XRD texture measurement conducted on a (10 mm^2) area.

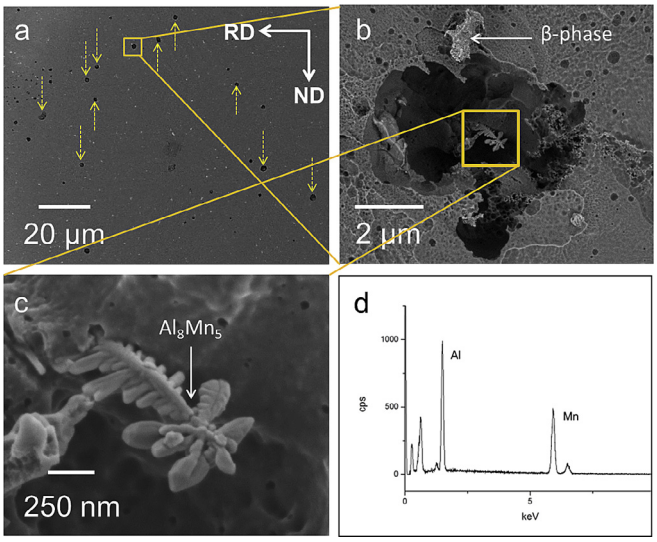

Fig. 3. (a) Backscattered electron micrograph of the alloy surface along with the corrosion products, after immersion in 3.5% NaCl solution for 30 min. The arrows indicate corrosion initiation sites (arrowed), (b) a typical corrosion pit after removal of corrosion products, and (c) a high magnification image presumably showing a flower-shaped Al_8Mn_5 intermetallic in the site interior, evidenced by the Al-Mn-content from the EDS spectrum, shown in (d). The characterization highlights the inception of **Stage I** corrosion.

events, including the micro-galvanic corrosion occurring at localized sites on the alloy surface, followed by the development of filiform-like corrosion morphologies from these corroded sites along the dendrite arms can be summarized together as **"Stage I"** corrosion. The gradual progression of such corrosion fronts is eventually observed to cover the alloy surface, with a relatively shallow corrosion attack.

Although it is evident that the corrosion attack progresses laterally across the surface, the SEM images from the transverse sections revealed non-uniform corrosion attack occurring in Stage I, i.e. 2 h immersion, which is shown in Fig. 4b. These were chosen as representative regions as observed from the top surface. Type A grains showed a corrosion depth of ~35 μm while Type B grains showed a corrosion depth of ~55 μm. Further, immersion tests in 3.5% NaCl for 24 h revealed that the corrosion depths varied significantly. An example of the corrosion depths measured for grains 1, 2 and 3 shown in Fig. 4b were 115 μm, 97 μm and 196 μm respectively. It is interesting to note that the corrosion morphologies in individual grains are significantly different, where grain 1 and grain 3 show deeper corrosion penetration, while grain 2 showed relatively uniform and laterally spread corrosion morphology with reduced corrosion depth. This event has been referred to as **"Stage II"** corrosion.

Therefore, it is considered that **Stage I** corrosion is mainly a consequence of the influence of the cathodic intermetallic phases on the anodic Mg microstructure. The corroded surface shows evidence of local micro-galvanic corrosion, which subsequently shows development of filiform-like corrosion morphologies across the alloy surface. As the non-uniform corrosion depths in individual Mg grains (Fig. 4b) observed in **Stage II** corrosion indicate a difference in the corrosion attack in Mg grains with different crystal orientations, the reason for the difference in corrosion propagation rates of individual Mg grains will be explored in the next section.

3.3. The crystallographic influence on corrosion

As evident from the corrosion depths in Fig. 4b corrosion propagates unevenly from grain to grain. Here this is investigated using electron backscattered diffraction in order to identify the relationship between the crystal orientation and corrosion rate in individual grains in **Stage I** corrosion.

3.3.1. Corrosion initiation

Fig. 5a shows a backscattered electron image of the corroded surface after 1 h of immersion, along with the crystal orientations of the α-Mg grains. The measurement of corrosion depths from each Mg grain has been undertaken using a 3D Bruker profilometer.

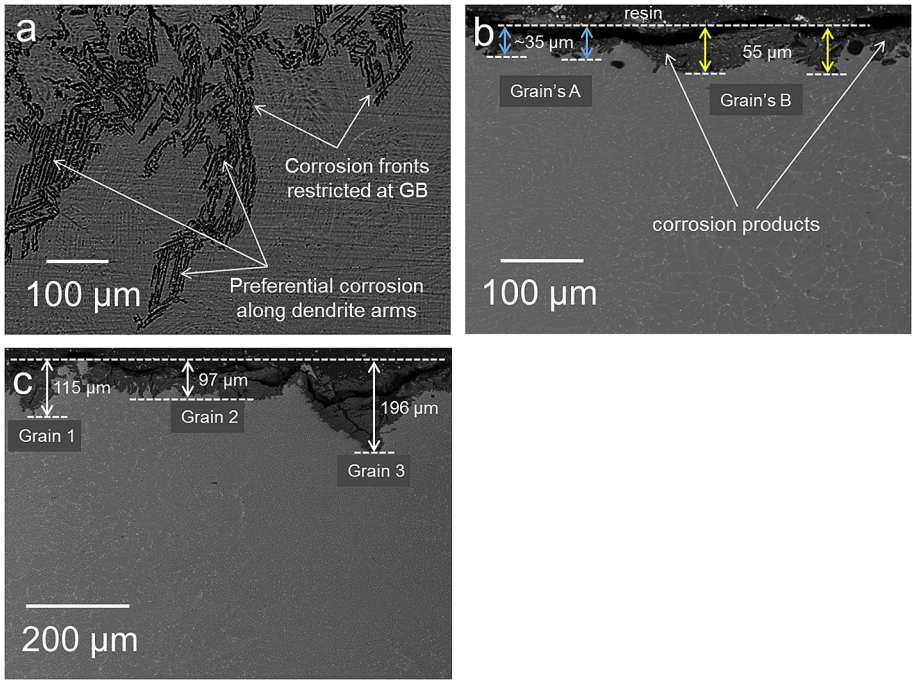

Fig. 4. SEM images of the corroded alloy specimen after immersion in 3.5% NaCl. (a) the top view after 2 h reveals preferential corrosion in the alloy matrix following the dendrite arms in the form of lateral filiform-like corrosion fronts (**Stage I**), (b & c) the transverse sections which reveal variable corrosion depths, suggesting non-uniform corrosion attack in individual Mg grains after 2 h **(Stage I)** and 24 h (**Stage II**). These were chosen as representative regions as observed from the top surface.

The threshold for the measurement of corrosion depths was considered with respect to the unexposed specimen edge. The α-Mg grains are assigned to two sets, where set (A1-A8) comprises grains having non-basal crystal orientations and set (B1-B8) those grains with basal crystal orientations. From the graph of the corrosion depths, shown in Fig. 5b, it is clear that on average the grains in set (A1-A8) show corrosion to greater depths (~52 µm), compared to those in set (B1-B8) (~26 µm). The α-Mg grains representing non-basal crystal planes are referred as $G_{(NB)}$ while those with basal or near-basal crystal orientations are referred as $G_{(B)}$ in the following text. This suggests that the severity of attack suffered by $G_{(NB)}$ is on average twice that for $G_{(B)}$.

The extent of corrosion from grain to grain varies widely, as is clear from Fig. 5c, where regions in red indicate shallow and reduced corrosion while regions in blue indicate increased corrosion depths. $G_{(B)}$ (1) shows relatively uniform corrosion, with an average corrosion depth of ~2 µm (Fig. 5d), whereas $G_{(NB)}$ (2) suffers from severe corrosion attack, with an average depth of ~31 µm (Fig. 5e). At the same time, it is interesting to note from the 3D images (Fig. 5d and e) that the resulting surface profiles of the two grains appear to be substantially different. This suggests that the Mg dissolution/corrosion in $G_{(B)}$ (1) is relatively uniform compared to $G_{(NB)}$ (2), which shows a deep, filiform-like corrosion attack and hence increased Mg dissolution (Fig. 5e). Clearly, the corrosion depth measurements coupled with the EBSD analyses after Stage I indicate that the crystal orientation significantly affects the Mg dissolution in individual Mg grains. To investigate the influence of crystal orientation after **Stage II**, a detailed microscopic analyses using a similar approach was conducted.

3.3.2. Corrosion propagation

Subsequently, the alloy surface shows the formation of corrosion products, usually $Mg(OH)_2$, **post-Stage I.** The breakdown of $Mg(OH)_2$ layer was observed [39], which was accompanied by spontaneous and vigorous H_2 evolution, an indication of the triggering of Stage II corrosion. This event was visually observed and the corroded specimen was characterized, where the **Stage II** corrosion had occurred after 24 h immersion testing. The filiform-like corrosion morphologies were clearly evident from the corroded surface, as shown in Fig. 6a. The severely attacked regions show an average depth of ~160–180 µm, while the surrounding surface shows shallow corrosion with an average depth of ~75 µm (measured using a 3D Bruker profilometer). The lateral propagation of corrosion fronts from the severely corroded areas appears to progress via the dendrite arms (arrowed). When observed under polarized light in the optical microscope (Fig. 6b), this region comprises several Mg grains (some are labelled in Fig. 6a), which were severely attacked. Hence, it is crucial to determine the typical crystal orientations of preferentially corroded Mg grains. At the same time, the influence of etching can be observed at some grain boundaries with corrosion cracks. It is important to note that the optical characterization of the corroded specimen was performed after storing in the desiccator, hence additional corrosion features are apparent that can be ignored for the moment. From a structural integrity perspective these demand further investigation going forward.

The band contrast map (Fig. 7a) shows dark features on the corroded surface which highlight the preferentially corroded areas during **Stage II**, while the inverse pole figure map (Fig. 7b) highlights the crystal orientations of respective Mg grains. The crystal orientations of the corroded Mg grains, evident in the EBSD map, have been considered to discuss the correlation between the crystal orientation and the corrosion propagation mechanism. The indexed EBSD patterns and crystal orientations for some corroded Mg grains have been highlighted in Fig. 7 (c1-c3), (d1-d3) and (e1-e3), which confirms that preferentially corroded grains 1–3, 5, 6 & 8 show non-basal crystal planes while grains 4 & 7 exhibit a basal or near-basal crystal planes. From the statistical analyses performed on the corroded areas, it was evident that the population of corroded non-basal Mg grains was significantly higher compared to the Mg grains with the basal planes parallel to the surface. Secondly, the corroded non-basal Mg grains typically showed increased corrosion depths

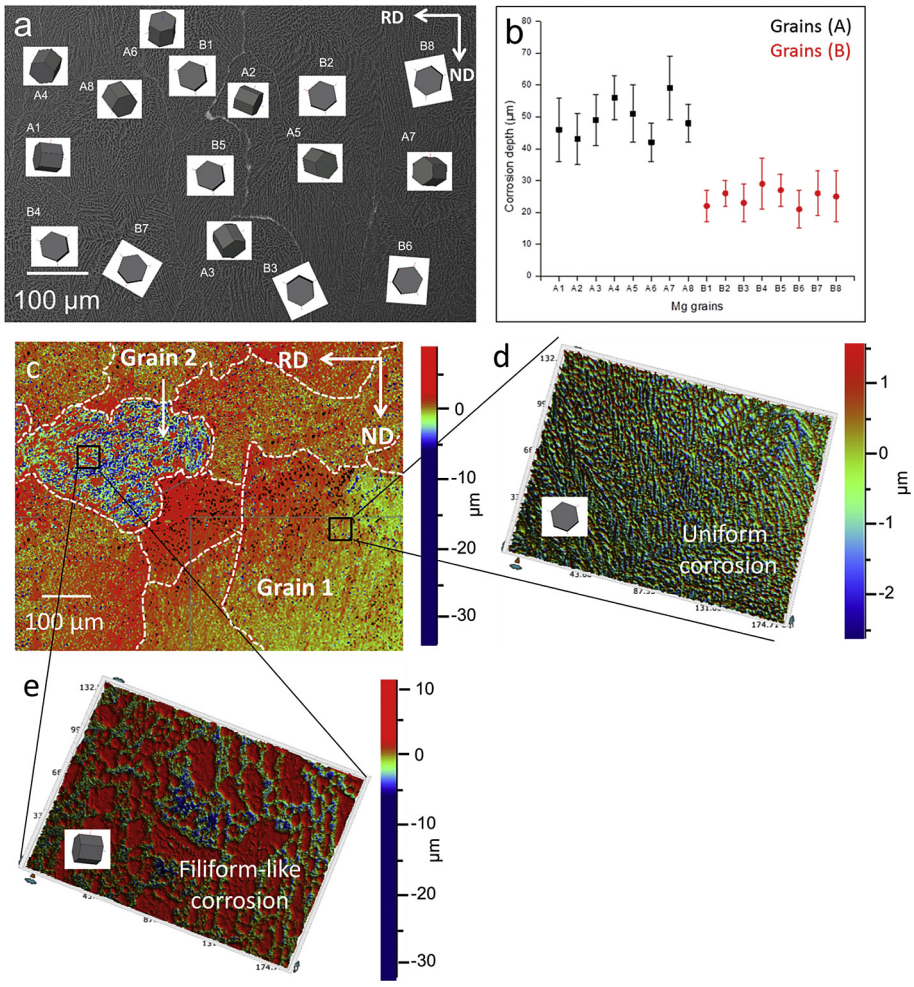

Fig. 5. (a) Characterization of the corroded surface after 1 h immersion (**Stage I)** and removal of corrosion products, using EBSD. The Mg grains are represented as two sets, (A1-A8) comprises Mg grains in non-basal crystal orientations and (B1-B8) those having basal/near-basal orientations, (b) graph shows average corrosion depths measured by optical profilometer for each Mg grain, (c) profile of the corroded surface after removal of corrosion products highlighting the variation in corrosion depth in individual Mg grains. (d) grain (1) shows shallow and uniform corrosion attack whereas (e) grain (2) exhibits filiform-like corrosion with increased corrosion depth (note different colour scales).

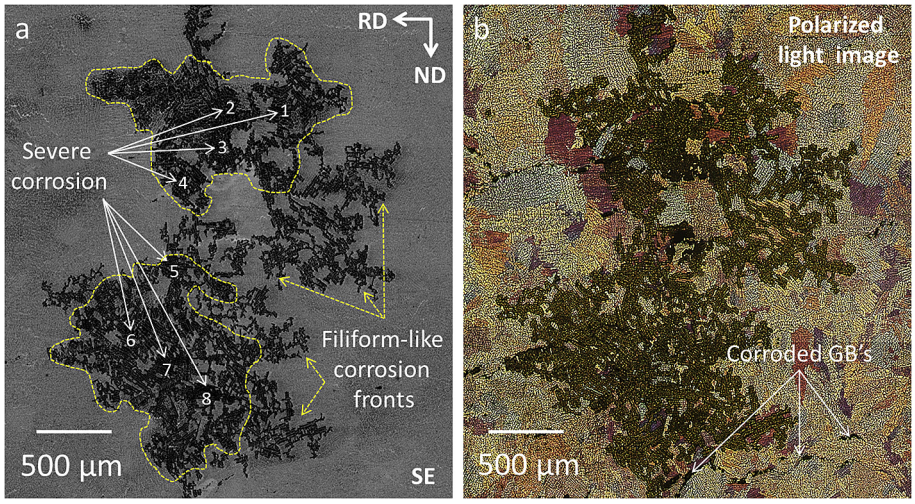

Fig. 6. (a) Back scattered electron micrograph of corroded surface after 24 h immersion (**Stage II)** reveals severely corroded regions (dark areas) and lateral filiform-like corrosion fronts, emanating from severely corroded sites, (the grains marked here are identified in Fig. 7). The surrounding surface is also affected from the corrosion attack; although not evident in low magnification and (b) plane polarized light image of the same region shows Mg grains with a wide range of crystal orientations. Some grain boundaries, highlighted in the image seem to be preferentially attacked, which can be attributed to etching (artifact).

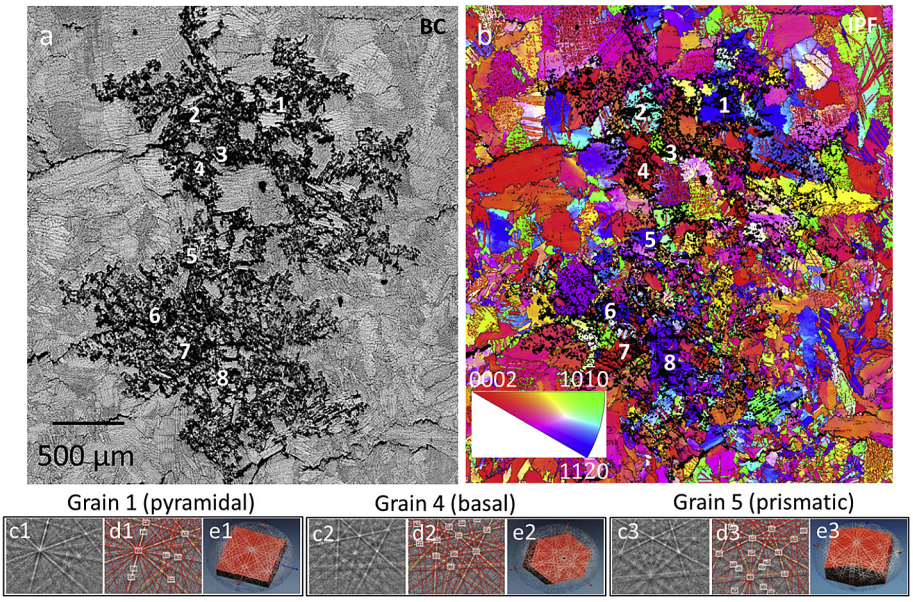

Fig. 7. EBSD characterization of the corroded surface shown in Fig. 6, after 24 h immersion (**Stage II**). (a) Band contrast map reveals the dark, severely corroded areas and (b) inverse pole figure (IPF) map, which shows the crystal orientations of the Mg grains, (c1-c5) electron backscattered diffraction patterns, (d1-d5) indexed patterns and (e1-e5) crystal orientations, of some of the severely corroded Mg grains.

compared to the basal Mg grains, also observed in **Stage I** (Fig. 5). This observation therefore confirms that the crystallographic influence on the sequential development of corrosion is extended from **Stage I** to **Stage II** and is expected to continue upon further exposure. The in-depth microscopic characterization of corroded areas from Stage II, shown in the micrograph, will be considered in

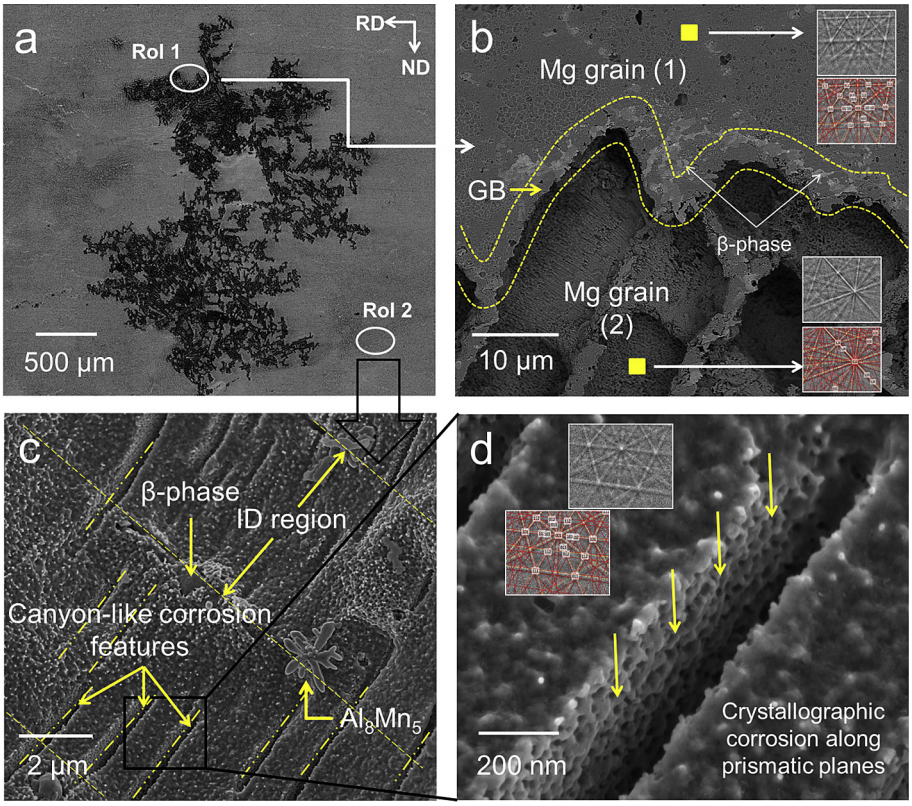

Fig. 8. Multiscale image comprising (a) low resolution composite backscattered electron micrograph of the corroded surface after 24 h immersion (**Stage II**) showing a region of severe corrosion one having negligible corrosion, (b) high magnification SEM image from the highly corroded region of interest (RoI1) showing the boundary between two Mg grains. EBSD confirms Grain 1 in (0002) orientation and Grain 2 in $(01\bar{1}0)$ orientation (c) exploded image from RoI2, exhibiting very shallow and uniform corrosion attack, with valley-like corrosion features across the interdendritic regions and remnants of Al_8Mn_5 intermetallics and β-phase and (d) higher magnification image of RoI2 displaying the canyon-like corrosion features, preferentially propagating along the prismatic plane.

the next section.

3.4. Characterization of corrosion features in individual Mg grains on the surface

In order to obtain further evidence related to the corrosion propagation in individual Mg grains with basal and non-basal crystal orientations after **Stage II**, the corrosion features have been probed by HR-SEM. Prior to the microscopic analyses, the corrosion products were removed from the corroded sample surface.

3.4.1. Mg grains in non-basal orientations

The microstructural analyses from a region of interest (RoI1) in Fig. 8a is shown in the high magnification image (Fig. 8b), which reveals the grain boundary interface between the adjacent α-Mg grains. In the image, Grain 1 displays shallow corrosion, whereas Grain 2 shows a severe corrosion attack along the dendrite arms, with the interdendritic boundaries largely unaffected. These act as a corrosion barrier to the corrosion taking place within the grain interior. At the same time, the grain boundary, highlighted with dotted lines in Fig. 8b, shows a significant amount of β-phase, which appears to confer additional resistance to the progression of the corrosion fronts at the grain boundary. EBSD reveals that $G_{(B)}$ (1) exhibits an [0002] crystal orientation while $G_{(NB)}$ (2) shows a [01$\bar{1}$0] crystal orientation confirming that higher Mg dissolution in Grain 2 can be associated with the typical non-basal crystal orientation [23–26].

3.4.2. Mg grains in basal orientations

Fig. 8c shows higher resolution analysis of $G_{(B)}$ in [0002] orientation, which suffered from a shallow corrosion attack (region of interest RoI2 in Fig. 8a). It is evident from the relatively flat corrosion morphology that the grain interior suffered macroscopically uniform corrosion attack. However, the corrosion morphology is significantly different from that observed in the corroded Mg grain of non-basal orientation (Fig. 8b). It is interesting to note the nanoscopically deep, crystallographic, canyon-like corrosion features within the remnant Mg matrix at high magnification (Fig. 8d). These canyons propagate into the grain interior, along the prismatic planes, beneath the corrosion products. The parallel sided, canyon-like corrosion features are located at ~90° to the interdendritic boundaries, which are highlighted by dotted lines in Fig. 8c [36]. The canyon-like corrosion features are observed across the interiors of dendritic cells in several corroded $G_{(B)}$'s. Therefore, this result suggests that the $G_{(B)}$'s exhibiting higher corrosion resistance [24–28], evident from the shallow corrosion depth (~75 μm) show preferential corrosion propagation along the prismatic crystal planes (Fig. 8d). At the same time, there is no evidence of corrosion propagation surrounding the cathodic phases like Al_8Mn_5 and β-phase (Fig. 8c).

4. Discussion

The current study typically highlights the influence of TRC microstructure on the corrosion properties of AZ31 Mg alloy sheet. Electron microscopy of the alloy surface shows cathodic phases namely, Al_8Mn_5, β-$Mg_{17}(Al,Zn)_{12}$, along with isolated Fe-particles (Fig. 1). The influence of the relatively high cooling rates associated with the TRC process [28], is clearly evident from the fine particle sizes of Al_8Mn_5 and β-phases (Fig. 1). Secondly, rolling, which is an integral part of the TRC process also dominates the distribution of the crystal planes of the Mg grains in the solidified microstructure (Fig. 2). From the EBSD results, it was confirmed that the surface exhibits a higher fraction of Mg grains of basal orientation (Fig. 2). Therefore, the discussion is based on the influence of local chemistries of microconstituent phases and crystal orientation of Mg grains which directly affects the corrosion at

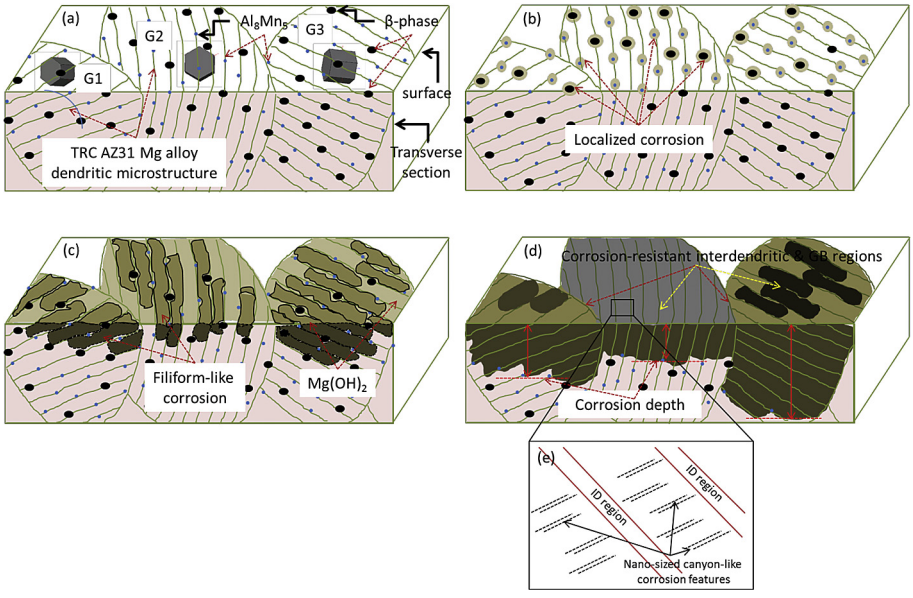

Fig. 9. Schematic diagrams showing the corrosion mechanism in TRC AZ31 Mg alloy in 3.5% NaCl solution. The surface indicates the 3D crystal orientations w.r.t. RD, whereas the transverse section microstructure reveals corrosion depths. (a) image reveals G1 (near-basal), G2 (basal) and G3 (non-basal) crystal orientations, along with the micro-constituent features, (b) corrosion initiation occurs at local sites constituting Al8Mn5/β/Fe particles (cathodes), (c) filiform-like corrosion fronts develop from the initiation sites and follow the dendrite arms. Both (b) and (c) constitute **Stage I** corrosion, (d) subsequent immersion shows corrosion propagation with increase in corrosion depth as a function of immersion time, which constitutes **Stage II** corrosion. The filiform-like corrosion fronts are observed in both G1 and G3 which indicate increased and preferential corrosion. G3 with non-basal crystal orientation shows increased corrosion depth followed by G1 with near-basal crystal orientation, while G2 with basal crystal orientation reveals a relatively uniform and reduced corrosion depth and (e) the exploded view of the corrosion occurring beneath the corrosion product in G2 (basal) grain which shows nano-sized, canyon-like corrosion features.

different stages. A schematic diagram (Fig. 9) is displayed in order to explain the sequential corrosion events.

4.1. Schematic representation of the corrosion events

Fig. 9a shows the TRC AZ31 Mg alloy microstructure, with Mg grains with crystal orientations, namely G1 (near-basal), G2 (basal) and G3 (non-basal), relative to RD (surface). On immersion, the corrosion initiates at localized cathodic sites, namely Fe-, Al_8Mn_5 and β-$Mg_{17}(Al,Zn)_{12}$, resulting in H_2 evolution and formation of corrosion products on the TRC surface, mainly, $Mg(OH)_2$, as shown in Fig. 9b. Further, lateral development of filiform-like corrosion fronts, which initiate from the local corrosion sites and follow the dendrite arms (Fig. 4a), preferentially consuming the Mg matrix. These corrosion fronts are restricted at the Al- and Zn-rich interdendritic/grain boundaries, highlighted in Fig. 9c. The localized micro-galvanic corrosion shown in Fig. 9b and the filiform-like corrosion morphologies in Fig. 9c together constitute Stage I corrosion event. Prolonged immersion shows propagation of corrosion fronts in individual Mg grains (Fig. 9d), evident in G3 & G1, which is significantly higher compared to G2, refers to Stage II corrosion. The difference in the corrosion depths is highlighted with the colour contrast of the $Mg(OH)_2$ corrosion product in individual dendrite arms, the Mg grains, and also being observed from the extent of corrosion attack on the cross section. Following with the high resolution microscopy shown in Fig. 9e, nanoscopically deep, crystallographic corrosion features, develop beneath the corrosion products, indicating the corrosion propagation in Mg grains with basal crystal planes.

4.2. Micro-galvanic corrosion

The role of intermetallics on the initiation of corrosion in TRC AZ31 Mg alloy has been reported earlier by the authors [10], and derives from the localized nobility of micro-constituent phases. Scanning Kelvin probe force microscopy (SKPFM) analyses on the TRC AZ31 Mg alloy sheet confirmed that the local Volta potential difference was capable of generating micro-galvanic coupling between the micro-constituents including Fe-particles, Al_8Mn_5 intermetallics and β-$Mg_{17}(Al,Zn)_{12}$ phase and the Mg matrix, which leads to the corrosion initiation (Fig. 3). The influence of intermetallic phases, mainly Al_xMn_y and the β-phase, on the corrosion behaviour of Mg-Al based alloys has also been widely reported; such phases act as cathodes, and, are responsible for micro-galvanic corrosion [9–11]. The results from short exposure times during the immersion experiments in the current study (Fig. 3), revealing localized corrosion are in good agreement with the literature. Following the localized corrosion initiation on the surface, consequent filiform-like corrosion fronts emerge, connecting the local corrosion sites within the dendrite arms, as a result of the anodic Mg dissolution. Lateral progression of the corrosion paths, which are restricted by the interdendritic boundaries, relative to the Mg matrix, can be attributed to the corrosion resistant Al-and Zn-rich coring. Such corrosion morphologies are a commonly observed phenomena in Mg-Al based Mg alloys [9–11].

4.3. Crystallographic orientation dependence

Although the corrosion fronts were observed to laterally cover the alloy surface, the cross sections showed variation in the corrosion depths (Fig. 4b). Referring to the initial corrosion depths (Fig. 5b), coupled with the crystal orientation of the Mg grains (Fig. 5a), it is clear that $G_{(NB)}$'s showed increased rates of corrosion propagation which in turn indicate faster Mg dissolution (Fig. 5c); compared to $G_{(B)}$'s (Fig. 5d). From the appearance of remnant surfaces (3D profilometric analyses), it is clear that $G_{(NB)}$'s suffer a non-uniform and localized corrosion attack (Fig. 5e) compared to $G_{(B)}$'s which exhibit a relatively uniform corrosion attack (Fig. 5d). Therefore, the difference in the resultant corrosion morphologies observed in both $G_{(B)}$'s and $G_{(NB)}$'s shed valuable insight on the mode of corrosion attack and the anodic Mg dissolution mechanism of Mg grains with a difference in the crystal planes. As mentioned in the introduction, for the case of pure polycrystalline Mg, the Mg dissolution rates in $G_{(B)}$'s were considerably slower compared to $G_{(NB)}$'s. This effect was attributed to the closely packed crystallographic plane (0001) and its lower surface energy, resulting in reduced Mg dissolution [23]. Saradha et al. [37] had reported that the theoretical work function value of a closely packed crystallographic plane was significantly more positive than that of a less closely packed plane, which was further experimentally confirmed by Song et al. [23]. Although the work function values have not been confirmed in the current study, the experimental findings here strongly support the hypothesis proposed by Saradha et al. The OCP of the metal is linearly correlated to the work function, which has been theoretically deduced and experimentally verified by authors elsewhere [23,29,38,39]. The non-uniform corrosion attack observed in the current study can be attributed to the influence of the TRC process on the surface, which constitutes a high fraction of $G_{(B)}$'s along with a random distribution of $G_{(NB)}$'s (Fig. 2). The consequent effect of crystal orientation of the Mg grains with different crystal planes is evident from the corrosion morphologies (Fig. 5) is similar the reported literature [23,24]. Prolonged exposure showed increased corrosion depths in Mg grains with crystal planes other than (0002) observed in the current study (Fig. 8). Hagihara et al. [26] recently examined the orientation-dependent corrosion behaviour of pure-Mg single crystals. The corrosion rates increased in the order $(0001) < (11\bar{2}0) < (10\bar{1}0) < (11\bar{2}3) < (10\bar{1}2)$. The dynamic polarization curves showed that the orientation-dependence of the current density was significant in the anodic region, while it was almost negligible in the cathodic region. Therefore, it was reported that the anodic reaction governs the orientation-dependent corrosion behaviour and that the charge-transfer and film resistances were strongly orientation-dependent.

Importantly, striated corrosion features were specifically observed on (0001) crystal planes in the case of pure Mg, when exposed to 3.5% NaCl [25,36]. However, it needs to be considered that the sample surfaces were examined along with the corrosion products; hence, it is quite possible that the corrosion morphologies beneath the corrosion products were not clearly evident. It was suggested that there was an underlying crystallographic influence on the development of surface structures. The evidence of preferential Mg dissolution along prismatic crystal planes in $G_{(B)}$'s was clearly evident from the current study (Fig. 8c–d) which suggests that the striated corrosion features must be connected and resemble to the canyon-like features observed in the current study and drive the corrosion propagation in $G_{(B)}$'s [25].

5. Conclusions

1. Corrosion initiation occurred preferentially at local sites, due to micro-galvanic coupling between the cathodic phases, namely: Al_8Mn_5 intermetallic particles, β-$Mg_{17}(Al,Zn)_{12}$ particles and the anodic Mg matrix in the dendrite arms. Subsequently laterally spread, filiform-like corrosion morphologies were observed across the alloy surface, consuming the Mg matrix along the dendrite arms, and the corrosion fronts being restricted at the Al- and Zn-rich interdendritic and grain boundaries. After immersion in 3.5% NaCl for 1 h, α-Mg grains with non-basal plane

on the surface showed an average depth of corrosion twice that of the α-Mg grains with {0002} planes on the surface.
2. Prolonged immersion in 3.5% NaCl showed non-uniform corrosion depths in individual Mg grains. EBSD characterization of the TRC surface confirmed that the corrosion propagation in non-basal Mg grains is pronounced compared to Mg grains of [0002] orientation.
3. For the Mg grains with {0002} planes on the surface, nanoscale, deep, crystallographic, canyon-like corrosion features had developed into the alloy perpendicularly, confirming that corrosion in such grains propagates preferentially along the prismatic planes.

Acknowledgements

The authors are grateful to the TARF-LCV Grant (EP/I038616/1), LiME Hub (EP/N007638/1) and the LATEST2 Programme Grant (EP/H020047/1). PJW is grateful for funding through an European Research Council Advanced Grant 695638 (CORREL-CT). The authors would like to acknowledge EPSRC funding for the Henry Moseley X-ray Imaging Facility under grants EP/M010619, EP/K004530, EP/F007906, EP/F028431.

References

[1] G.L. Makar, J. Kruger, Int. Mater. Rev. 38 (1993) 138–153.
[2] G. Song, A. Atrens, Adv. Eng. Mater. 5 (2003) 837–858.
[3] J.D. Hanawalt, C.E. Nelson, J.A. Peloubet, Trans. AIME 147 (1942) 273.
[4] G.S. Frankel, A. Samaniego, N. Birbilis, Corr. Sci. 70 (2013) 104–111.
[5] S. Feliu Jr., A. Samaniego, A.A. El-Hadad, I. Llorente, Corr. Sci. 67 (2013) 204–216.
[6] H. Matsubara, Y. Ichige, K. Fujita, H. Nishiyama, K. Hodouchi, Corr. Sci. 66 (2013) 203–210.
[7] F. Cao, Z. Shi, J. Hofstetter, P.J. Uggowitzer, G. Song, M. Liu, A. Atrens, Corr. Sci. 75 (2013) 78–99.
[8] J. Liao, M. Hotta, S. Motoda, T. Shinoharra, Corr. Sci. 71 (2013) 53–61.
[9] A. Pardo, M.C. Merino, A.E. Coy, R. Arrabal, F. Viejo, E. Matykina, Corr. Sci. 50 (2008) 823–834.
[10] S. Pawar, X. Zhou, G.E. Thompson, G. Scamans, Z. Fan, J. Electrochem. Soc. 162 (9) (2015) C442–C448.
[11] S. Pawar, X. Zhou, G.E. Thompson, J.D. Robson, I. Bayandorian, G. Scamans, Z. Fan, Corrosion 68 (6) (2012) 548.
[12] J.T. Carter, R. Verma, P.E. Krajewski, Magnes. Technol. (2008) 69–74.
[13] R. Verma, J. Carter. SAE Paper 2006-01-0525.
[14] P.E. Krajewski, S. Kim, J.T. Carter, R. Verma, Magnesium sheet: automotive applications and future opportunities, Korean Inst. Metals Mater. Trends Metals Mater. Eng. 20 (5) (2007) 60–68.
[15] S. Das, N. Barekar, O.E. Fakir, X. Yang, J.P. Dear, Z. Fan, Mater. Lett. 144 (2015) 54–57.
[16] I. Bayandorian, Y. Huang, Z. Fan, S. Pawar, X. Zhou, G.E. Thompson, Metall. Mater. Trans. A 43 (2012) 1035–1047.
[17] Y.S. Park, S.B. Lee, N.J. Kim, Mater. Trans. 44 (2003) 2617.
[18] S. Das, N.S. Barekar, O.E. Fakir, L. Wang, A.K. Prasada Rao, J.B. Patel, H.R. Kotadia, A. Bhagurkar, J.P. Dear, Z. Fan, Mater. Sci. Eng. A 620 (2015) 223–232.
[19] H. Men, B. Jiang, Z. Fan, Acta Mater. 58 (2010) 6526–6534.
[20] M. Masoumi, F. Zarandi, M. Pekguleryuz, Mater. Sci. Eng. A 528 (2011) 1268–1279.
[21] N. Tang, M.P. Wang, H.F. Lou, Y.Y. Zhao, Z. Li, Mater. Chem. Phys. 116 (2009) 11–15.
[22] F. Kaiser, J. Bohlen, D. Letzig, K.-U. Kainer, A. Sfyczynski, C. Hartig, Adv. Eng. Mater. 5 (12) (2003) 891–896.
[23] G. Song, R. Mishra, Z. Xu, Electrochem. Commun. 12 (2010) 1009.
[24] G. Song, Z. Xu, Corr. Sci. 54 (2012) 97–105.
[25] M. Liu, D. Qiu, M.C. Zhao, G. Song, A. Atrens, Scr. Mater 58 (2008) 421.
[26] K. Hagihara, M. Okubo, M. Yamasaki, T. Nakano, Corr. Sci. 109 (2016) 68–85.
[27] B.-Q. Fu, W. Liu, Z.-L. Li, Appl. Surf. Sci. 255 (2009) 9348–9357.
[28] G.-L. Song, Z. Xu, Corr. Sci. 63 (2012) 100.
[29] P. Schmutz, V. Guillaumin, G.S. Frankel, R.S. Lillard, J.A. Lillard, J. Electrochem. Soc. 150 (2003) B99–B110.
[30] C.R. McCall, M.A. Hill, R.S. Lillard, Corros. Eng. Sci. Technol. 40 (2005) 337.
[31] R.S. Lillard, G.F. Wang, M.I. Baskes, J. Electrochem. Soc. 153 (2006) B358–B364.
[32] ASTM-G31-12a. 2012; http://dx.doi.org/10.1520/G0031-12A.
[33] ASTM-G1. 2011; http://dx.doi.org/10.1520/G0001-03R11.
[34] S. Pawar, X. Zhou, T. Hashimoto, G.E. Thompson, G. Scamans, Z. Fan, J. Alloys Compd. 628 (2015) 195.
[35] Y. Yang, F. Scenini, M. Curioni, Electrochim. Acta 198 (2016) 174–184.
[36] L. Yang, X. Zhou, M. Curioni, S. Pawar, H. Liu, Z. Fan, G. Scamans, G. Thompson, J. Electrochem. Soc. 162 (2015) C362–C368.
[37] R. Saradha, M.V. Sangaranarayana, J. Phys. Chem. B 102 (1998) 5099–5106.
[38] M. Stratman, H. Streckel, Corr. Sci. 30 (1990) 681–696.
[39] P. Schmutz, G.S. Frankel, J. Electrochem. Soc. 145 (1998) 2285–2295.